Chapter 2

Thermal and thermoelastic design of cryogenic silicon microstrip detector modules

2.1 Design of cryogenic detector modules

A module is the basic building block in a silicon tracker detector system, and should integrate the silicon sensor and its readout electronics. The design of a module for the Large Hadron Collider (LHC) experiments is constrained by the requirements on radiation hardness, minimal mass and low multiple scattering. The starting point of the design of a cryogenic module are naturally the modules of ATLAS and CMS, which feature radiation hardness up to the neutron equivalent fluence of $3 \cdot 10^{14}$ cm^{-2}, and are presently the most radiation-hard and fastest tracking detectors.

The ATLAS modules are double sided, with single-sided silicon microstrip sensors mounted back-to-back on a heat spreader spine, whose role is to provide thermal stability to the fully irradiated sensors when they are operated at a temperature of about –10 °C [14]. The spine conducts the sensor heat load to the cooling point of the module, which is at the same time a precision mounting point. The cooling point interfaces with a cooling block, through which two-phase C_3F_8 flows inside 4 mm cooling pipes. In the CMS modules, the sensors are mounted on a heat sink cooled on its sides by 2 mm pipes through which single-phase C_6F_{14} is flowing [15].

ATLAS uses radiation-hard DMIL front-end readout chips, whereas CMS has CMOS chips made in radiation-hard 0.25 µm deep sub-micron (DSM) technology. The CMOS electronics performs well at much higher fluences than the design ones and therefore we have chosen the CMS module as the basis for the new module design, which is described below.

The goal of the RD39 Collaboration is to improve the radiation hardness by a factor of 10 by operating the detectors at cryogenic temperatures. This requires improved thermal and thermomechanical performance of the module since neither the ATLAS nor the CMS modules can be cooled below their operating design temperatures without risks. Due to the different thermal dilatation of the various materials used in those modules, the thermal stresses developed during cool-down would lead to the camber of the sensors, to the peeling of Kapton®, and ultimately to the fracture of the most fragile components, such as the sensors. The large stress induced at the silicon can be reduced to a minimum if silicon is glued on silicon or on another material matching its thermal dilatation, using only a thin layer of epoxy. Because silicon has a very high thermal conductivity, such glued structures are not sensitive to thermal shock either.

Operation at low temperatures enables to reduce the mass of the module. Rather than cooling through a heat spreader and a high conductivity support plate on which the cooling tube is mechanically clamped, our module is cooled by a microtube that is directly integrated under the pitch adapter. The hybrid[1] (main heat source) and the sensor are thus separated thermally. The use of two-phase evaporative cooling makes possible the use of capillary pipes down to 200 µm diameter. No additional heat spreader is required for the sensor thanks to the increased thermal conductivity of silicon and because of the low leakage current at low temperatures.

Cryogenic module components and alignment

The key features of our prototype single-sided modules are given in Figure 2.1, which shows how the main components and the ears for mechanical alignment and support are integrated together. These elements are the silicon sensor, the readout electronics, the pitch adapter[2] and the cooling pipe. The choice of the component materials for a cryogenic module is guided by the properties of the silicon sensors, and the main criteria include thermal dilatation, thermal conductivity and elastic properties, in addition to the radiation resistance (Section 2.2).

The components are assembled by glue on a support plate using alignment tooling (Section 2.5). The design is such that in mass production the components could be assembled with a pick-and-place robot. The module features three alignment and attachment ears which are glued onto the support plate and machined on the extensions of the spacer sitting under the pitch adapter.

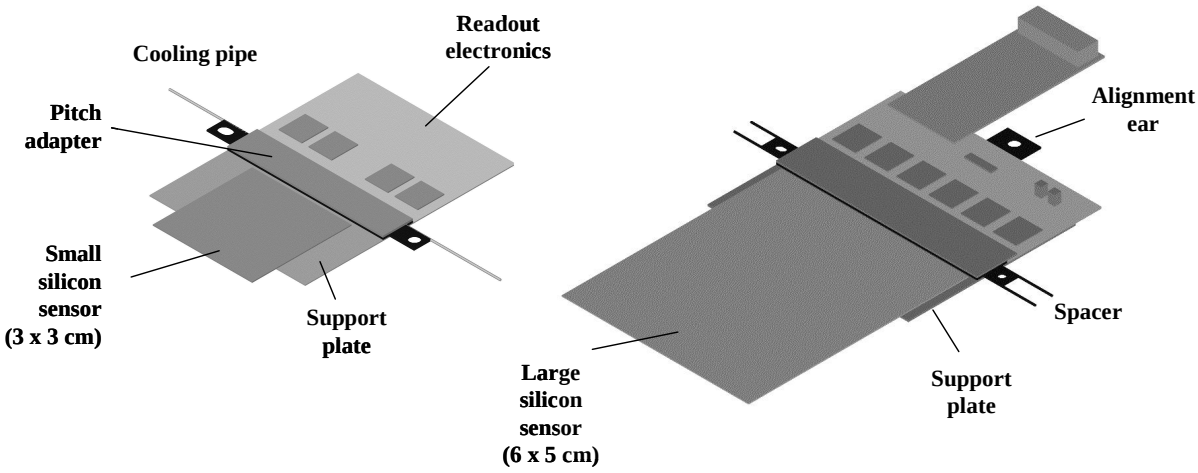

Figure 2.1 Module with a small sensor (left), complying with the CERN TOTEM experiment specifications [14] and module with a large sensor, which could be used in the central trackers of the LHC experiments. The main components to be integrated in a module are the silicon microstrip sensor, the readout electronics, the pitch adapter and the cooling pipe.

1 Hybrid is an electronic component integrating the readout (APV25) and control chips.
2 The pitch adapter is an intermediate element that matches the silicon microstrip sensor pitch to that of the readout chips.

A first module was designed according to specifications defined by the CERN TOTEM experiment [14], which planned to use such cryogenic detectors in Roman pots very close to the LHC beam. The dimensions shown in Table 2.1 correspond to such a module, which hosts a small silicon sensor of 3 x 3 cm^2 active area. A module with a large sensor of 5 x 6 cm^2 active area, which could be used in the central trackers of the LHC experiments, was also designed and produced at a later stage (see Chapter 5). Both modules are shown in Figure 2.1.

Table 2.1 Component dimensions of a module with a small sensor.

Element	Dimensions
Detector	30 x 30 x 0.3 mm^3
Support plate	47 x 63 x 0.3 mm^3
Pitch adapter	47 x 9 x 0.3 mm^3
Readout electronics	47 x 30 x 0.3 mm^3
Micropipe	0.6 mm OD / 0.5 mm ID
Spacer	47 x 9 x 0.55 mm^3
Glue Layers	100 μm thickness

Cooling

By using two-phase fluid cooling (Section 2.3), the module power, typically around 3 W, can be absorbed by a microtube embedded in the module structure as close as possible to the heat sources (readout electronics), as shown in Figure 2.2. This is possible because two-phase fluid cooling features a very high heat transfer coefficient (HTC) and a low pressure drop, and because the use of a fluid with a high latent heat of evaporation leads to a low mass flow rate (Section 2.4).

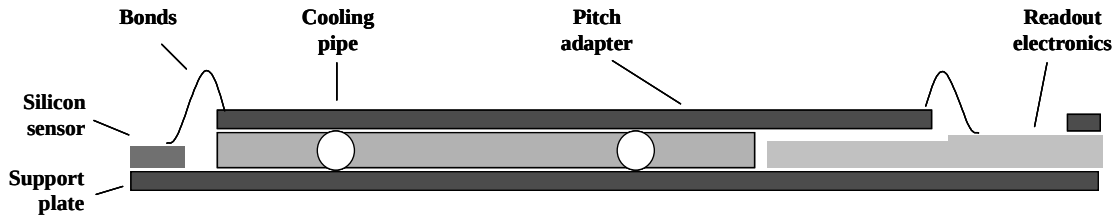

Figure 2.2 Cross-section of the carbon fiber composite (CFC) spacer where the cooling pipes are embedded.

First thermal simulations (Section 2.2) of the prototype detector modules suggest that the coolant flowing in a single microchannel inside the module needs to be at a temperature less than 10 K below the 130 K design temperature of the sensors; this leads us to the choice of argon and methane which are suitable coolants around 120 K temperature.

Engineering of support and vacuum systems

The main problems of a low-temperature precision tracker support structure are the stability and deformation under thermal stresses. As it is hardly possible to match its dilatation with that of silicon, it is necessary to relieve the thermal stresses between the modules and the support structure by providing the necessary elasticity at the fixing and alignment points. The structure could be made out of CFC in such a way that it has a very high thermal stability and nearly zero thermal dilation.

The modules will be placed in a warm vacuum chamber. A vacuum environment provides the cleanest possible conditions for the silicon detectors, which are sensitive to humidity and other contaminants. The cryogenic vacuum can be made particularly clean by using cryopumping panels in the critical areas. At the same time the metallic vacuum chamber works as a perfect Faraday cage and makes the control of electromagnetic interferences simple.

The mechanical supports linking the cold tracker to the room-temperature walls of the cryostat vacuum vessel must be made of low-conductivity materials such as glass-epoxy, which does not have zero dilatation. The dilatation can be compensated by using an active hydraulic correction system which provides fine control of the tracker position inside the vacuum vessel cavity.

Numerous vacuum feedthroughs are required for the cabling, and although the fabrication of epoxy sealed cryogenic vacuum feedthroughs is well mastered in a small scale, improved and automated fabrication techniques should be developed for a good large-scale yield.

2.2 Choice of materials

The choice of the materials for a cryogenic module is determined by the thermoelastic properties of the silicon sensors. Silicon has a low thermal dilatation which matches AlN ceramic almost perfectly down to 130 K, and is also compatible with sintered Al_2O_3 and with the Pyrex®[1] and silica glasses (Figure 2.4). The latter two have a low thermal conductivity and can be used for providing thermal isolation which may be useful in the pitch adapter between the silicon sensors and the readout electronics. The silica glass has almost zero dilatation between room temperature and 130 K, and matches zero-dilatation carbon fibre composites (CFC).

Silicon has an excellent thermal conductivity of 7 W cm^{-1} K^{-1} at 120 K (Figure 2.4). In order to achieve small temperature gradients and a uniform temperature distribution in the module, silicon could be used, not only for the microstrip detector itself, but also as a constructional material. This would also avoid the generation of mechanical stress or deformation during cool-down due to differences in thermal expansion (Figure 2.4). Therefore, both the support plate and pitch adapter could be processed in silicon. The high voltage (HV) insulation on these components would be provided by a SiO_2 layer grown when processing these components on silicon wafers.

1 Pyrex® (borosilicate 7740) is a trademark of Corning Glass Inc.

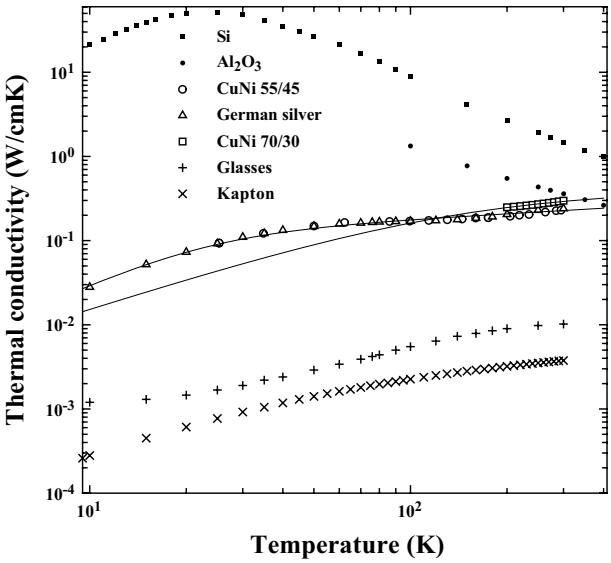

Figure 2.3 Thermal conductivity of materials often used in silicon detector modules.

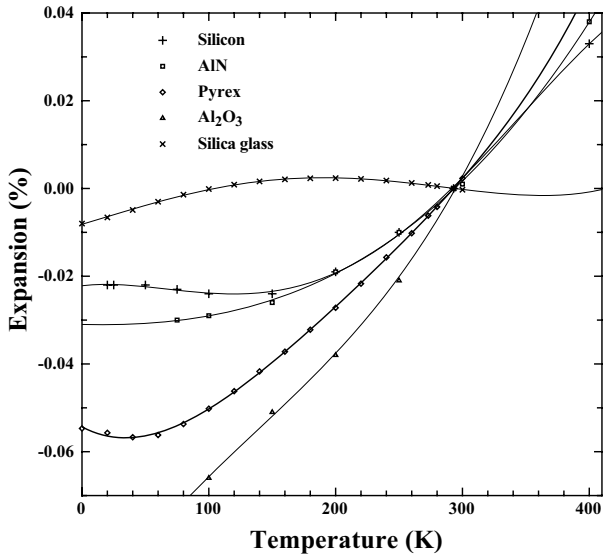

Figure 2.4 Thermal expansion of materials often used in silicon detector modules.

The readout hybrid can be assembled either on silicon or Al_2O_3 ceramic, which is glued to the support plate. Future design options may feature hybrids processed using thick-film techniques on silicon. The entire module could be built out of this material by integrating the cooling into microchannels directly micromachined into the hybrid support [16]. Then the pitch adapter could be also printed on the silicon hybrid.

The cooling micropipe is clad in a CFC structure between the hybrid and the silicon sensor; this technique allows to match the larger thermal expansion of the pipe material with that of silicon, and the geometry yields a good thermal separation between the electronics and the sensor (Figure 2.2). The

cooling micropipes of our modules have 0.6 mm outer diameter and 50 µm wall thickness, and they are made of 70/30 CuNi. The appropriate materials for the construction of a cryogenic module are summarized in Table 2.2.

Table 2.2 Component materials that can be used in a silicon module.

Element	Material
Detector and front-end integrated circuits	Silicon
Support plate	sintered Al_2O_3 ceramic
Pitch adapter	AlN ceramic
Hybrid circuit board	Pyrex® or silica glasses silicon
Micropipe	70/30 CuNi
Spacer	Carbon fiber composite
Glue Layers	Stycast® 1266 Stycast® 2850FT Araldite® 2011 Type L epoxy

In order to define the final geometry and materials for the module, its thermal behavior was analyzed using finite element modeling in ANSYS[1]. Below, material properties, geometry, boundary conditions and temperature distributions resulting from these simulations are presented.

Material properties

Few data are available on the thermoelastic properties of materials as a function of temperature in literature. The compilations of Brookhaven National Laboratory [17] and Touloukian [18] are the main sources which have been used. The thermal conductivity and integral thermal dilatation as a function of temperature for materials often used in the construction of silicon detector modules are shown in Figure 2.4. These are the data used in our simulations.

Since the integral thermal dilatation of the epoxy is a key factor in the thermoelastic design, measurements for specific radiation-hard epoxies were carried out at CERN. The chosen epoxies were Araldite® 2011 (Ciba)[2], Stycast® 1266™ (E&C)[3] and Type L epoxy[4] (R&G) from 300 K to 4.2 K. The Young modulus and tensile strength, which also have a strong dependence with temperature, were also measured for the three previously mentioned epoxies at 77 K and 300 K. These measurements are described in detail in Chapter 3.

1 ANSYS, Inc. Version 5.7, 2003
2 Araldite® is a registered trademark of Huntsman Advanced Materials (Switzerland) GmbH. Huntsman produces and distributes Araldite® 2011.
3 Stycast® is a registerd trademark of National Starch and Chemical Company. Emerson and Cuming produces and distributes Stycast® 1266.
4 R&G Faserverbundwerkstoffe GmbH.

Regarding the thermal conductivity of the epoxy, and due to the lack of data, the value at room temperature is used for the full temperature range. This is somehow optimistic, since the thermal conductivity of amorphous materials decreases with decreasing temperature.

The carbon fiber composite (CFC) spacer where the cooling pipe is embedded was made out of 6 layers of fibers oriented perpendicularly with respect to the adjacent ones[1]. Therefore the matrix can be considered to be isotropical in the plane of the layers (x,y) and anisotropic in the perpendicular component (z). According to D.J. Radcliffe and H.M. Rosenberg [19], the conductivity of the composite along the fibres is given by:

$$\lambda = V_f \lambda_f + (1 - V_f)\lambda_m , \tag{2.1}$$

where V_f is the volume concentration of fibre and λ_f and λ_m are the thermal conductivities of the carbon fiber and epoxy respectively. The thermal conductivity perpendicular to the fiber axis (theory of Lord Rayleigh) can be calculated as:

$$\lambda = \lambda_m \left[1 - \frac{2V_f}{\nu + V_f - \frac{3V_f^4}{\nu^2 \pi^4} S^2} \right] , \tag{2.2}$$

where

$$\nu = \frac{\lambda_m + \lambda_f}{\lambda_m - \lambda_f} \tag{2.3}$$

and $S = 0.032\ \pi^4$.

For our specific application, the Thornel®[2] K1100X 2K graphite fiber was used. The longitudinal thermal conductivity at room temperature of this fiber is estimated to range from 950 W m^{-1} K^{-1} to 1170 W m^{-1} K^{-1} (2 to 3 times higher than that of copper). This composite was chosen for components where effective heat transfer, light weight and radiation hardness are required. The prepeg has a fibre volume ratio of 60 %.

According to Equation 2.1, 2.2 and 2.3, the composite thermal conductivity at room temperature along the x and y axes is therefore about 600 W m^{-1} K^{-1} and 0.8 W m^{-1} K^{-1} along the z-axis. Since the temperature dependence of neither the epoxy nor the fibre are known, the thermal conductivity is assumed to be constant.

A summary of the most significative thermoelastic properties of the materials, as they are used in the finite element simulation, is presented in Table 2.3.

1 The carbon fiber composite plate was produced by the CERN AT group.
2 Thornel® is a registered trademark of Amoco Performance Products, Inc. U.S.A.

Table 2.3 Thermoelastic properties of materials often used in silicon microstrip detector modules.

	Density at RT ρ (kg/m^3)	**Thermal conductivity λ (W m^{-1} K^{-1})**	**Coefficient of thermal expansion γ(K^{-1})**	**Young Modulus *E* (GPa)**
Silicon	2330	148 (300 K)[a] 884 (100 K)	2.6 10^{-6} (293 K)[a] -0.4 10^{-6} (100 K)	112.4 (300 K)[b]
Al_2O_3	3970	36 (300 K)[a] 133 (100 K)	5.4 10^{-6} (293 K)[a] 0.6 10^{-6} (100 K)	370 (300 K)
AlN	3260	1.75 (300 K)[a] 6.30 (100 K)	2.5 10^{-6} (293 K)[a] 0.5 10^{-6} (100 K)	---
Kapton®	1420	0.38 (300 K)[c] 0.23 (100 K)	22.2 10^{-6} (293 K)[d]	2.9 (300 K)[e] 3.5 (77 K)
Pyrex®	2230	1.1 (300 K)[a] 0.69 (100 K)	2.8 10^{-6} (293 K)[a] 1.5 10^{-6} (100 K)	63 (300 K)
CFC		600 (parallel) 0.8 (perp.)	assumed to be zero	
70/30 CuNi	8940	29.8 (300 K) 21.9 (100 K)	15.0 10^{-6} (293 K)[f] 11.2 10^{-6} (100 K)	140 (300 K)[g]
Araldite® 2011	1050	0.22 (300 K)[h]	8.8 10^{-5} (293 K)[i] 4.3 10^{-5} (130 K)	1.8 (300 K)[i] 14.3 (77 K)
Stycast® 2850GT	2290	1.36 (300 K)	27.4 10^{-6} (300 K)	---
Stycast® 2850FT	2300-2500	1.36 (300 K)	29 10^{-6} (300 K)	7.5 (300 K)
Stycast® 1266	1120[j]	assumed equal to that of Araldite® 2011	7.06 10^{-5} K^{-1} (293 K)[i] 3.5 10^{-5} K^{-1} (130 K)	3.2 (300 K)[i] 11.0 (77 K)
Type L epoxy	1010[k]	assumed equal to that of Araldite® 2011	6.55 10^{-5} K^{-1} (293 K)[i] 3.5 10^{-5} K^{-1} (130 K)	2.6 (300 K)[i] 15.5 (77 K)

a. Y.S. Toulokian, Thermophysical properties of matter [18].
b. Silicon Casting, Inc.
c. D. L. Rule, D. R. Smith and L. L. Sparks, Thermal conductivity of a polymide film between 4.2 and 300 K, with and without alumina particles as filler [20].
d. Private communication with E. Serafini, Du Pont.
e. M. Davidson, S. Bastian and F. Markley, Measurement of the elastic modulus of Kapton® perpendicular to the plane of the film at room and cryogenic temperatures [21].
f. Values for 65% Copper - 35% Nickel alloy.
g. Values for 90% Copper - 10% Nickel alloy.
h. Ciba Chemical Specialties technical data sheet.
i. γ and *E* of Araldite®, Stycast® and Type L epoxy have been measured at CERN (Chapter 3).
j. Emerson & Cuming technical data sheet.
k. R&G technical data sheet.

Geometry and meshing of the finite element model

The first module thermal simulations were performed with a simplified geometry meshed with hexahedral cells. In this model (see Figure 2.5) all the key components are represented: support plate, readout electronics, silicon microstrip sensor, pitch adapter, spacer and cooling pipes. The model has about 40000 elements and 51000 nodes. The spatial resolution is 0.5 mm at the cooling pipe zone and 1 mm at the rest of the mesh.

The spacer, shown in detail in Figure 2.5, was simulated with a simplified model here[1]. In this case, the cooling pipe is cast into epoxy. To guarantee the horizontallity of the pitch adapter, which is sitting on top of the cooling pipe, a silicon spacer is glued to the support plate at the opposite end. The silicon element has the same height as a dent on the hybrid, which is the second support point for the pitch adapter. From the cooling pipe a direct path is established towards the hybrid (the main heat source) and another one through the support towards the detector.

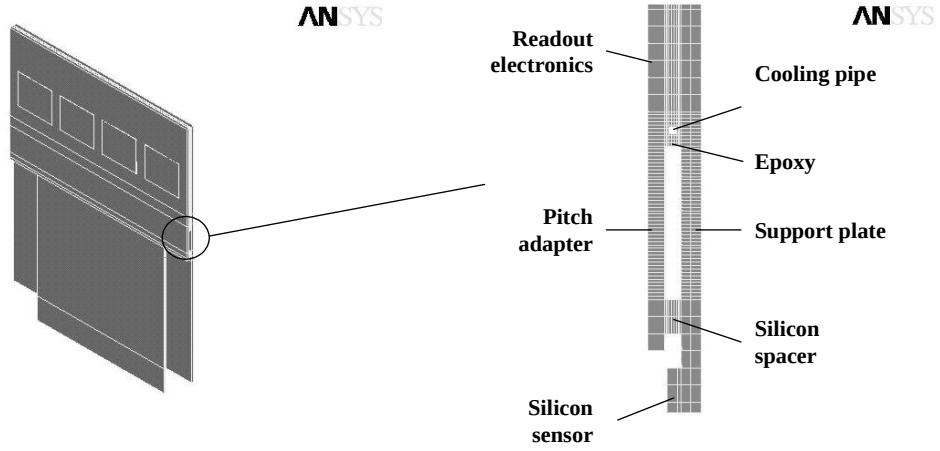

Figure 2.5 Volumes (left) and detail of spacer (right) of the finite element model.

Heat Loads

Operating reverse-biased silicon sensors at 130 K entails a negligibly small bulk leakage current in the sensor, and consequently there is no heat generated in the sensor itself. Heat loads are therefore mainly due to the readout electronics power dissipation and thermal radiation from the vacuum chamber to the cold module.

The CMS CMOS chip APV25[2] will be used for the readout electronics. The APV25 is a 128 channel chip with each channel dissipating 2.31 mW. Therefore, the heat load per double-sided module with 10 readout chips is about 3 W. In the simulation only a half-module with 4 chips is modeled.

1 The carbon fiber spacer described in the first section of this chapter is modeled accurately in simulations performed later to compare to thermal tests performed in a mechanical module, shown in Chapter 4.

2 APV25 User Guide, v.2.2, 2001 (http://www.te.rl.ac.uk/med).

Thermal radiation transports heat between the vacuum chamber, which is at room temperature, and the detector module cooled at 130 K. To calculate this thermal load, a good approximation is to use the diffuse-gray surface enclosure hypothesis [22]:

$$\dot{Q} = \frac{\sigma A_1 (T_1^4 - T_2^4)}{\frac{1}{\varepsilon_1} + \frac{A_1}{A_2}\left(\frac{1}{\varepsilon_2} - 1\right)} \quad , \tag{2.4}$$

where $\dot{Q}$ is the radiation heat load, σ is the Stefan-Boltzmann constant (5.670 10^{-8} W/m^{2}K^4), A_1 and A_2 are the silicon module surface at T_1 (130 K) and the roman pot inner surface (considered to be a cylinder of 100 mm inner diameter) at T_2 (300 K), ε_1 and ε_2 are the total hemispherical emissivities of $\varepsilon_{Al} = 0.06$ for the aluminium pot and $\varepsilon_{Si} = 0.19$ for silicon at their respective temperatures. Using this expression, one module of the dimensions shown in Table 2.1 would absorb a thermal radiation heat load of about 235 mW.

Heat loads were applied onto the finite element model as heat flux boundaries, with the APV25 power dissipation of 4 x 300 mW applied on their bottom surfaces and the overall radiation heat load of 235 mW equally distributed on all surfaces.

The heat sink was defined with a fluid bulk temperature circulating through the cooling pipe at either 110 K or 120 K. A conservative heat transfer coefficient of 10^4 W/m^{2}K was used.

Temperature distribution

Several material combinations were simulated in order to study the thermal behaviour of the module in each case and particularly determine the temperature distribution along the silicon sensor. Different geometries for the spacer where the cooling pipe is embedded were modeled, depending on whether one or two pipes were used. Simulations where the carbon fiber composite spacer is modeled and with better accuracy of the geometry of the cooling pipe were prepared to compare to the thermal tests results carried on a mechanical module. These simulations are presented in Chapter 4.

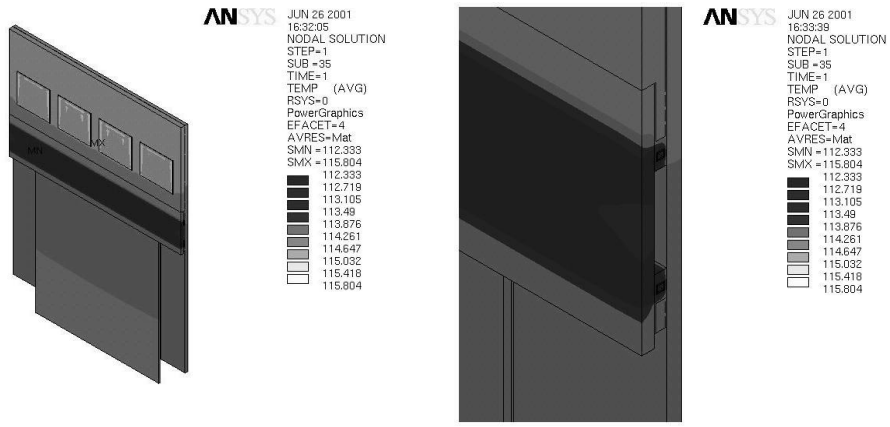

Figure 2.6 The temperature distribution of the module is shown for a geometry with two cooling pipes, silicon support plate and detector, alumina ceramic readout electronics, Pyrex® pitch adapter, Stycast® 2850 GT glue layers and Kapton® film.

Usual materials for the pitch adapter are glass materials such as Pyrex®, while the readout electronics is often printed using thick-film techniques on alumina ceramic (Al_2O_3). Such materials were used in the first simulations. The support plate and sensor are made out of silicon. A Kapton®[1] polymide film is used to insulate the back plane of the silicon sensor. All the components are glued together using 50 μm layers of Stycast® 2850 GT, which is a high thermal conductivity epoxy filled with Al_2O_3 powder[2] (the thermal conductivity is considered to be 1.54 W m^{-1} K^{-1}).

The results (see Figure 2.6) show how the maximum temperature difference (with respect to the bulk temperature of argon) is less than 6 K at the APV25 and less than 5 K at the silicon sensor when two cooling pipes are used. As expected, the largest thermal gradients are located within a small area around the cooling pipes, which are surrounded by epoxy with low thermal conductivity. On the contrary, the temperatures of the support plate and detector are nearly uniform because of the high thermal conductivity of silicon.

The same simulation was performed with a single cooling pipe, the maximum ΔT being in this case of the order of 10 K. The sensor is marginally colder than the electronics. This exercise proved that a single pipe could provide enough cooling to keep the sensor at 130 K.

In order to demonstrate the importance of a good heat spreader at the support plate, a simulation using AlN for this component was performed. The temperature distribution can be seen in Figure 2.7. In this case, larger gradients are observed along the support plate. The maximum ΔT is of 18.6 K, i.e., nearly 10 K more than in the case where silicon is used for the support plate.

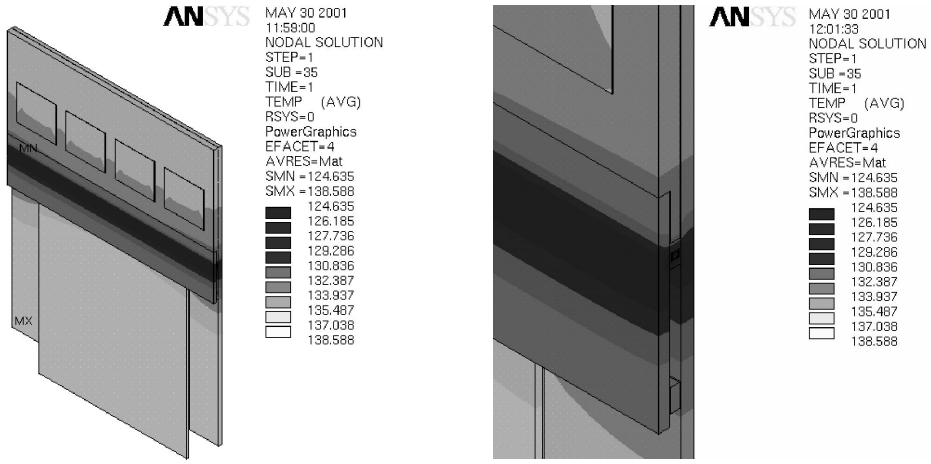

Figure 2.7 The temperature distribution of the module is shown for a geometry with one cooling pipe, AlN support plate, silicon detector, alumina ceramic readout electronics, Pyrex® pitch adapter, Stycast® 2850 GT glue layers and Kapton® film.

Since the goal is to obtain a temperature distribution which is as uniform as possible, it seems that a module made entirely out of silicon would be the best solution. Building a module in silicon would also have the advantage of avoiding thermal dilatation mismatch between the components, and consequently minimize thermal stresses and deformation.

1 Kapton® is a registered trademark of E.I. du Pont de Nemours and Company.
2 Private conversation with O.Ramseier, Emerson & Cuming, Sept. 2001

Such a module was simulated, the temperature distribution being in this case the one shown by Figure 2.8. The uniformity all along the module can be observed. In this case, the maximum temperature difference between the fluid saturation temperature and the readout electronics is about 8.5 K. The silicon sensor has a temperature of about 127 K and the hybrid is only marginally warmer.

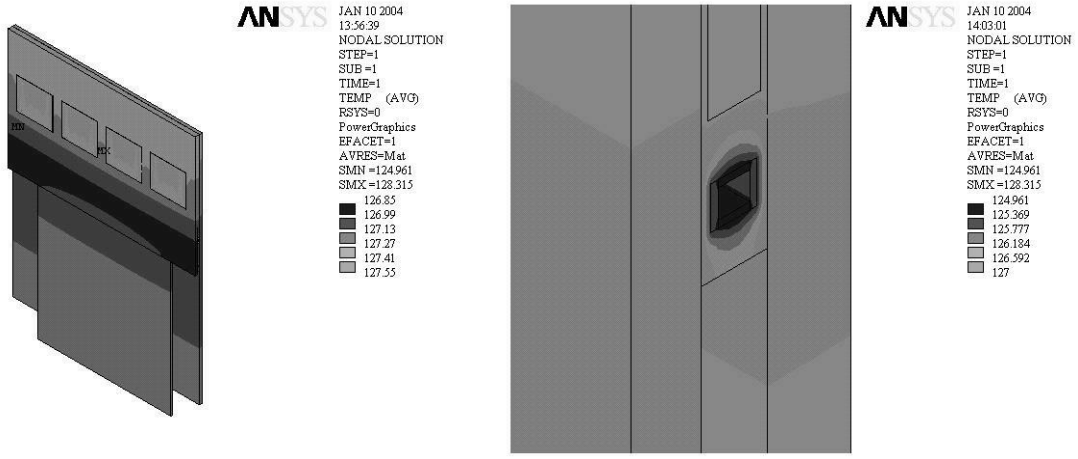

Figure 2.8 The temperature distribution of the module is shown for a geometry with one cooling pipe, silicon support plate, detector, readout electronics and pitch adapter, Stycast® 2850 GT glue layers and Kapton® film.

All the materials, boundary conditions and results of these simulations are summarized in the following table:

Table 2.4 Materials, boundary conditions and results of the thermal simulations.

	2 cooling pipes	**1 cooling pipe**	**AlN Support**	**Silicon Module**
Support Plate	Silicon	Silicon	AlN	Silicon
Pitch adapter	Pyrex®	Pyrex®	Pyrex®	Silicon
Hybrid	Alumina	Alumina	Alumina	Silicon
Epoxy	Stycast® 2850 GT	Stycast® 2850 GT	Stycast® 2850 GT	Stycast® 2850 GT
T_{Ar}	110 K	120 K	120 K	120 K
HTC	10^4 W/m^{2}K	10^4 W/m^{2}K	10^4 W/m^{2}K	10^4 W/m^{2}K
Max. ΔT	6 K	10 K	19 K	8.5 K

The regularity of the temperature along the module shown by the latter simulation favours silicon as a constructional material. The numbers shown here compare extremely favourably with the current microstrip module designs of ATLAS and CMS where the sensors are more than 10 K warmer than the fluid, and the readout ASICs are about 45 K hotter. A series of thermal tests (see Chapter 4) were performed to verify these thermal simulation results and validate the design principles.

2.3 Cooling system

Evaporative cooling by two-phase argon in capillary pipes

The cooling system design is determined by the requirements of the cryogenic modules. For our particular application in microstrip modules, a cooling power between 10 W and 100 W at temperatures around 100 K is needed[1]. Moreover, a minimized impact and mass contribution of the cooling system to the detectors are the main requirements. The cooling is to be provided by a closed circuit with autonomous operation, which should require maintenance intervals in the order of 1 to 2 years. Last but not least, the design must take into account that the distance between the cold source and the detectors is in the range of meters.

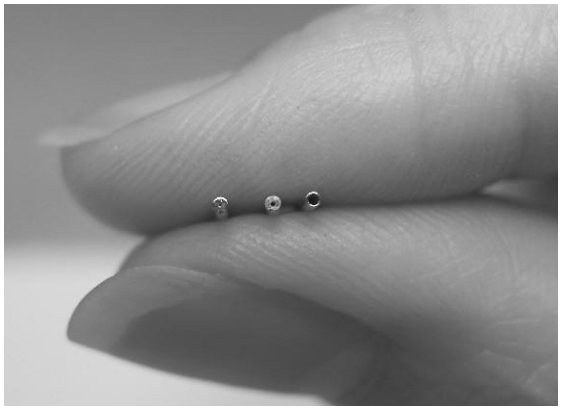

Figure 2.9 Microtubes of 800 μm outer diameter and 120, 250 and 500 μm nominal inner diameter used to cool silicon microstrip detector modules.

Miniaturized cryogenic fluid circuits with regenerative cryocoolers are ideal for cooling in our power range [23]. The best performance and highest degree of integration in a device is achieved with two-phase flow and forced circulation of the coolant. A room-temperature compressor (optionally a cryogenic micropump [24]) provides the circulation of the coolant through the circuit and the microtube heat exchangers.

Circuits can be designed with single-phase liquid flow or two-phase flow. Pure vapour cooling is characterized by a very low heat transfer coefficient α and low capacity flux ($\dot{C} = \dot{m} \cdot c_p$). Two-phase cooling systems use the latent heat of evaporation of the working fluid, and therefore require lower mass flow rates compared with single-phase liquid systems. An additional benefit is that temperature profiles in devices are smoother due to the almost constant evaporating temperature and to the very high heat transfer coefficient.

To cool silicon sensors down to 130 K, the most suitable fluid is argon with a saturation pressure of 15 bar at a saturation temperature of 124 K. The specific volume flow rate per unit of cooling power in such circuits is between 0.5 ml min^{-1} W^{-1} and 1.0 ml min^{-1} W^{-1}, which leads to flow channel diameters below 1 mm in heat exchangers.

1 Such cooling power corresponds to Roman Pot Stations (Chapter 1) requirements.

Fluid circuit with a warm compressor

The schematic diagram of a fluid circuit with a warm compressor and the thermodynamical cycle in the pressure-enthalpy (*p-h)* diagram for argon are shown in Figure 2.10. The circuit consists of a cold part and a warm part which are connected through an internal heat exchanger (IHX). Room temperature argon is circulated by the compressor from (1) to (2). An air heat exchanger cools the compressed gas to (3). The super-heated gas is then cooled and partially condensed to (4) in the internal heat exchanger. A condenser - receiver is connected to the cryocooler (heat sink) that absorbs the specific heat condensing and sub-cooling the fluid to (5).

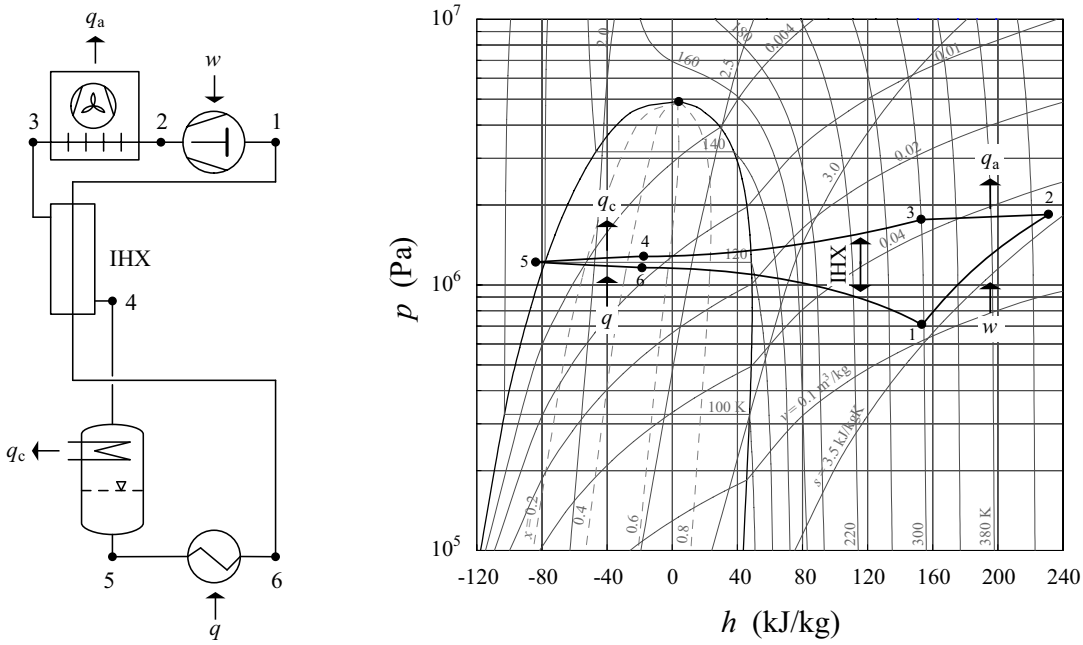

Figure 2.10 Warm compressor circuit scheme and cycle in the *p-h* diagram for argon.

Advantages of the compressor system are that this is an inexpensive solution with off-the-shelf components. Besides, a high power density and a pressure drop of several bar can be accepted in the heat exchanger. However, an efficient filtering system for oil and water removal is needed, which requires maintenance.

Design of a miniature evaporator heat exchanger for a cryogenic module

The design of microtube evaporator heat exchanger for cryogenic silicon detector modules is mainly determined by the length of the heat exchanger, by the number of modules in series and by the available pressure head.

One of the most important parameters in the design is the heat flux. Too low heat fluxes can cause instabilities in the transition from single-phase to two-phase flow. However, too large heat fluxes can cause critical boiling conditions. Besides, the heat transfer coefficient depends strongly on the heat flux. The mass flux and the quality (vapour fraction) have little influence on nucleate boiling heat transfer.

The available pressure head in our fluid circuit was in the order of 2 bar to 3 bar. For a heat exchanger of 47 mm length and for a module with 6 APV25 readout chips, a pressure drop of 0.07 bar (homogeneous flow model [25]) or 0.12 mbar (Storek & Brauer correlation [26]) is expected. Therefore, with such a pressure-head more than 10 modules could be connected in series with a cooling tube of 500 μm inner diameter.

2.4 Heat transfer measurements in microtubes

Modeling of local heat transfer coefficients in microtubes is essential for the design of evaporator heat exchangers that are integrated in the detector modules. Due to the lack of previous experimental data, experiments have been recently carried out with circular microtubes suitable for cooling cryogenic tracking detectors [27]. The experiments were focused on nucleate boiling dominated heat transfer, which is the common regime in the applications. However, the two-phase heat transfer measurements were preceded by single-phase measurements with liquid Argon in order to characterize and calibrate the test section of the microtube exchanger. The single-phase heat transfer coefficients are also needed in the correlations for the two-phase heat transfer coefficients. All these results are compared in Chapter 4 with experimentally evaluated heat transfer coefficients obtained in a series of thermal tests.

Single-phase heat transfer measurements

The results on single-phase (laminar and turbulent liquid, and turbulent vapour) heat transfer have shown that there is no physical difference in heat transfer mechanisms between macro tubes and microtubes [27]. The enhancement of heat transfer coefficients in microtubes compared to conventional correlations is explained with the increased influence of roughness, or the relative increase of the wetted surface compared to the volume.

A transversal section of the CuNi pipe used in our modules is shown in the microscopic image of Figure 2.11. Three measurements of the inner diameter (and roughness) are shown, yielding the diameters of 519, 528 and 526 μm.

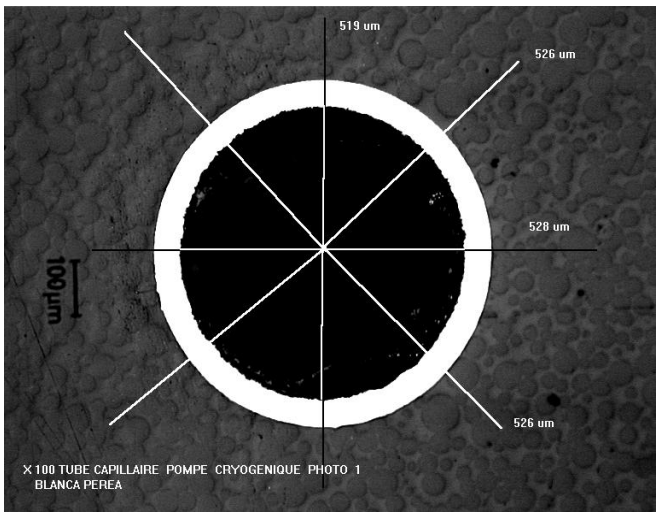

Figure 2.11 Microscopic image of the transversal section of the module cooling pipe, showing the inner diameter and roughness.

The mean heat transfer coefficient $\bar{\alpha}$ is defined as the heat load ($\dot{Q}$) divided by the wetted surface of the flow channel (A_w) and the mean temperature difference $\Delta T_{m,w}$:

$$\bar{\alpha} = \frac{\dot{Q}}{A_w \Delta T_{m,w}} \tag{2.5}$$

In single-phase flow $\Delta T_{m,w}$ is the logarithmic mean temperature difference:

$$\Delta T_{m,w} = \frac{T_{out} - T_{in}}{\ln\left(\frac{\bar{T}_w - T_{in}}{\bar{T}_w - T_{out}}\right)} \tag{2.6}$$

where T_{in}, T_{out} are the fluid bulk temperatures at the inlet and at the outlet of the heat exchanger and $\bar{T}_w$ is the mean temperature of the wetted surface.

The heat transfer in single-phase turbulent flow can be modeled using the Dittus and Boelter equation [28], which is valid for $Re > 10^4$

$$Nu = 0.0234 Re^{0.8} Pr^{0.4} , \tag{2.7}$$

where Nu is the Nusselt[1] number, Re is the Reynolds[2] number and Pr is the Prandtl[3] number.

In the transition region of $2300 < Re < 10^4$, the Hausen-type equation [29] is more precise:

$$Nu = H0 \cdot (Re^{H1} - H2) \cdot Pr^{0.4} \left[1 + \left(\frac{d}{L}\right)^{\frac{2}{3}}\right] K_T , \tag{2.8}$$

where d and L are the pipe diameter and length respectively. The coefficients and the parameter K_T have values of:

Gases ($0.5 < Pr < 1.5$)	H0 = 0.0214	H1 = 0.8	H2 = 100	$K_T = 1$
Liquids ($1.5 < Pr < 500$)	H0 = 0.012	H1 = 0.87	H2 = 280	$K_T = \left(\frac{\eta}{\eta_w}\right)^{0.11}$

1 The Nusselt number is $Nu = \frac{\alpha d_w}{\lambda}$, where α is the heat transfer coefficient [W/m^{2}K], d_w the wetted diameter [m] and λ the thermal conductivity [W m^{-1} K^{-1}].

2 The Reynolds number is $Re = \frac{\omega \rho d_w}{\eta}$, where ω is the velocity [m/s], ρ is density [kg/m^3], d_w the wetted diameter [m] and η the dynamic viscosity [Pa s].

3 The Prandtl number is $Pr = \frac{\eta C_p}{\lambda}$, where η the dynamic viscosity [Pa s], Cp is the specific heat at constant pressure and λ the thermal conductivity [W m^{-1} K^{-1}].

The heat transfer in microtubes at the transition region is better described by redefining H1 as H1 = 0.87 $r_d^{0.22}$ for liquids and H1 = 0.87 $r_d^{0.55}$ for gases [27]. r_d is the relative roughness parameter defined as:

$$r_d = \frac{d_w}{d_c}, \tag{2.9}$$

where d_w is the wetted diameter and d_c is the diameter of a perfectly smooth circular tube.

For laminar flow (Re < 2300), the mean heat transfer coefficient can be described following the correlation given in [28]:

$$\overline{Nu} = \left[\left(\frac{a}{1-n}\left(\frac{Re \cdot Pr \cdot d}{L}\right)^n\right)^3 + Nu_\infty{}^3\right]^{\frac{1}{3}} K_T \tag{2.10}$$

where the coefficients are:

$\dot{q}$ = constant	Nu_∞ = 4.364	a = 1.1	n = 0.35
T_w = constant	Nu_∞ = 3.656	a = 0.89	n = 0.35

K_T =1 for gases and $K_T = \left(\frac{\eta}{\eta_w}\right)^{0.11}$ for liquids.

The experimental mean heat transfer coefficients for single-phase laminar liquid flow (Reynolds numbers up to 2000) are smaller than 1700 W/m^{2}K [27]. Similar values are found for single-phase turbulent vapour flow (Reynolds numbers from 7000 to 20000). The mean heat transfer coefficients become higher (between 4000 W/m^{2}K and 7000 W/m^{2}K) for single-phase turbulent liquid flow (Reynolds numbers between 4500 and 8000). The experimental data for turbulent liquid and turbulent vapour flow is shown in Figure 2.12.

The single-phase heat transfer measurements allowed to calibrate the thermal resistance of the test section, which will be used later in the two-phase measurements. The roughness factor to be included in the correlation was also measured.

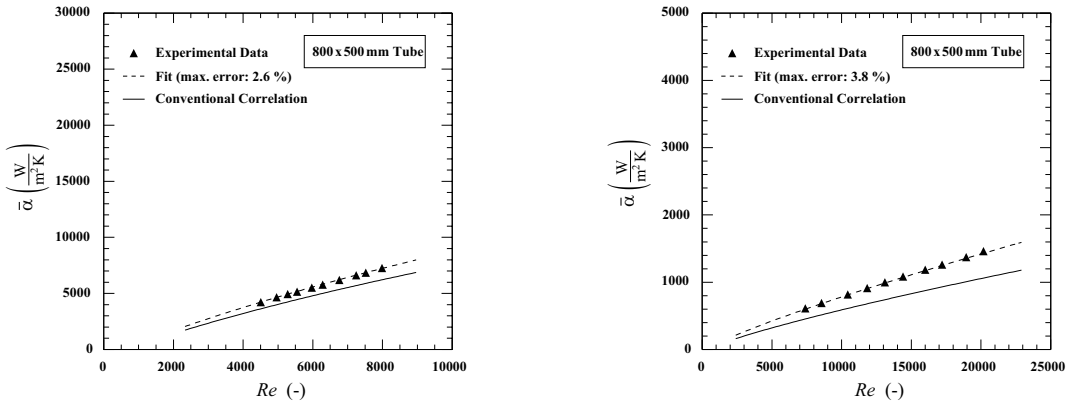

Figure 2.12 Heat transfer coefficients in single-phase turbulent liquid flow (left) and single-phase turbulent vapor flow (right), extracted from [27].

Two-phase heat transfer measurements

The local flow-boiling heat transfer coefficient α is calculated as a function of the local convective boiling heat transfer coefficient α_c and the local nucleate boiling heat transfer coefficient α_{nb}. The required heat flux for the onset of nucleate boiling, according to the VDI Heat Atlas [30] is:

$$\dot{q}_{onb} = \frac{2\sigma T_s \alpha_{l,0}}{r_{crit}\rho_v(h_v - h_l)} \quad , \tag{2.11}$$

where σ is the surface tension, T_s is the saturation temperature, $\alpha_{l,0}$ the single-phase liquid heat transfer coefficient at the same mass flux, r_{crit} is the critical radius, ρ_v the vapour density and h_v-h_l the latent heat.

If the heat flux is too small to activate nucleation centers ($\dot{q} < \dot{q}_{onb}$), then the flow regime is convective boiling, and the heat transfer coefficient depends strongly on the quality factor x, mass flux $\dot{M}$ and density ratio ρ_l/ρ_v. The correlation used to describe the local heat transfer in convective boiling in microtubes is the VDI Heat Atlas correlation for vertical tubes:

$$\frac{\alpha_c}{\alpha_{l,0}} = \left((1-x)^{0.01}\left[(1-x)^{1.5} + 1.9x^{0.6}\left(\frac{\rho_l}{\rho_v}\right)^{0.35}\right]^{-2.2} + x^{0.01}\left[\frac{\alpha_{v,0}}{\alpha_{l,0}}\left(1 + 8(1-x)^{0.7}\left(\frac{\rho_l}{\rho_v}\right)^{0.67}\right)\right]^{-2}\right)^{-0.5} \quad , \tag{2.12}$$

where $\alpha_{l,0}$ and $\alpha_{v,0}$ are local single-phase heat transfer coefficients, calculated for the case that the fluid was flowing at the same total mass flux in form of saturated liquid and saturated vapour, respectively (Equation 2.7 to Equation 2.10).

If nucleate boiling occurs ($\dot{q}_{onb} < \dot{q} < \dot{q}_{crit}$), it usually dominates and therefore modeling α_{nb} is very important. The experimental data on nucleate boiling regime show that there is no significant influence of the mass flux and the quality factor on the heat transfer coefficient. The nucleate boiling heat transfer model yields [27]

$$\frac{\alpha_{nb}}{\alpha_0} = C_F\left(\frac{\dot{q}}{\dot{q}_0}\right)^n\left[2.816p^{*0.45} + \left(3.4 + \frac{1.7}{1-p^{*7}}\right)p^{*3.7}\right]\left[\left(\frac{d_0 r_d}{d_c}\right)^{0.4}\left(1 - e^{-0.45\cdot\frac{d_c}{L}}\right)\right]\left(\frac{R_a}{R_{a,0}}\right)^{0.133} \quad , \tag{2.13}$$

where α_0 is the reference heat transfer coefficient in pool boiling at the heat flux $\dot{q}_0$ (for Argon these values are 3870 W/m^{2}K and 10000 W/m^2 respectively), C_F is a constant related to fluid properties (C_F = 0.91 fits well experimental data [27]), $\dot{q}$ is the heat flux, p^* is the reduced pressure (saturation pressure/critical pressure), d_0 = 0.01 m, d_c is the characteristic diameter, r_d is the relative roughness, R_a is the arithmetic mean roughness, $R_{a,0}$ = 1 μm, and n is:

$$n = 0.7 - 0.13\cdot 10^{0.48p^*} \quad . \tag{2.14}$$

Since the local nucleate boiling heat transfer coefficient does not depend on the quality factor, it is equal to the mean heat transfer coefficient. In the case of convective boiling, we have to integrate over the heat exchanger length to obtain the mean heat transfer coefficient. In two-phase flow, the mean heat transfer coefficient is defined by Equation 2.5 with the mean wall temperature difference:

$$\Delta T_{m,w} = \bar{T}_w - \bar{T}_{fl} \ , \tag{2.15}$$

where $\bar{T}_{fl}$ is the mean fluid temperature in the heat exchanger.

The experimental mean heat transfer coefficients for two-phase flow nucleate boiling regimes, measured in [27] range from 18000 W/m^{2}K to 36000 W/m^{2}K for total power ranging from $\dot{Q}$ = 1 W to 8 W.

The precision of the prediction of nucleate boiling heat transfer coefficients can never be better than ± 30 % to 40 % due to the fact that nucleate boiling flow regimes can be meta-stable. This effect is related to the number of active nucleation centers, which is influenced by the history of the flow. However, the main conclusion we should extract from the measurements in microtubes is that the heat transfer coefficients in two-phase flow are one order of magnitude higher than those measured in single-phase flow.

2.5 Alignment principles and design of the assembly tooling

There are two main aspects concerning the alignment of a module: the alignment of the module components with respect to each other; and the alignment of the modules with respect to the beam and to other detector modules.

The assembly of the components can be done, in principle, using precision tooling or with a pick-and-place robot in case of mass production. For prototype module assembly, precision gluing jigs were designed and produced. The tooling precision is given by the accuracy of the mechanical edges of the components and the positioning of the alignment pins, which is about 20 μm. The repeatibility of the system is better than 3 μm.

The alignment of the module with respect to the beam is done using a warm support plate, placed between the module and the vacuum chamber. The module is attached to this support structure through three thermally isolating precision support posts with dowels. These go through an alignment hole and a slot that are located on the carbon fiber spacer, and through a third point at the hybrid end, as shown by Figure 2.13. The alignment hole determines an (x,y) position of the module, while the slot fixes the rotation allowing movement along the x axis. The third alignment point does not constrain the coordinates x and y but fixes the module in its z component.

The position of the module and its readout strips is thus accurately referred to the vacuum chamber, which itself can be aligned in the test beam line using optical targets fixed to it.

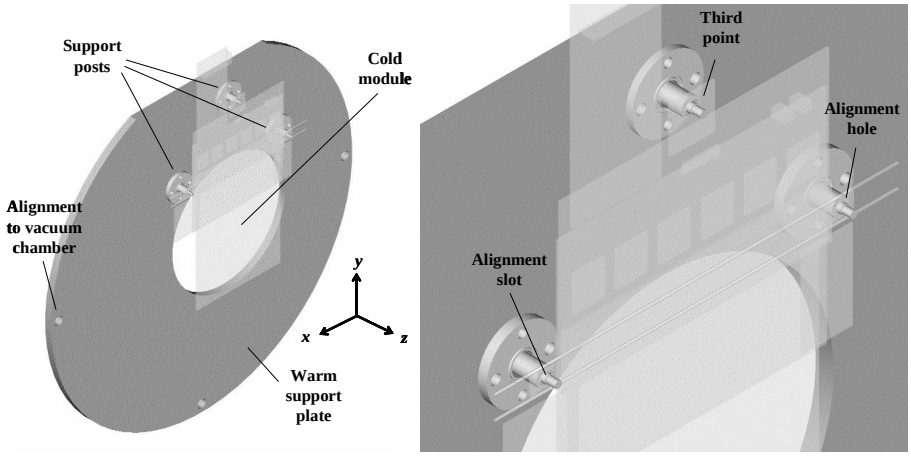

Figure 2.13 Schematic showing the principles of alignment of the cold module with respect to the beam and other detector modules, by using a warm support plate and three thermally isolating precision support posts with dowels.

Precision assembly of the module components with accurate alignment tooling

The assembly of the module is done using precision gluing jigs (Figure 2.14), based on positioning and transfer plates provided with vacuum lines to fix the components, and on precision pins to place them.

The base and transfer plates are positioned with respect to each other by two precision rods located on the base plate. As shown by Figure 2.15, two pins tangential to one of the rods fix the *(x,y)* position of the transfer plate with respect to the base plate. The rotation is fixed by another pin tangential to the second rod. Nylon screws are used to avoid deformation of the positioning rods.

In this prototype assembly tooling, the holes for the pins used to position the module components on the base plate, and the positioning plate itself are machined within a precision of 20 μm. The final alignment between the components depends on the precision of their edges. The whole assembly system has a reproducibility better than 3 μm. For final production of the modules, optical alignment could be used leading to a precision better than 3 μm in the component positioning and to independency on the precision of the edges.

All the surfaces that are in contact with active components are coated with Teflon®[1], on which the vacuum lines are machined to hold the components in place. Teflon® protects the components and glue does not adhere to it. The latter is important in case of glue overflow.

Different glue patterns have been studied by assembling glass modules. Two main parameters allow a good control of the gluing: the glue dispenser needle diameter and the applied pressure. By using a temporizer, the amount of glue on a dot pattern can be determined and reproduced with reasonable accuracy. The glue layer thickness is controlled by using precision shims, which are sandwiched between the base plate and transfer plates while gluing.

1 Teflon® is a registered trademark of E.I. du Pont de Nemours and Company.

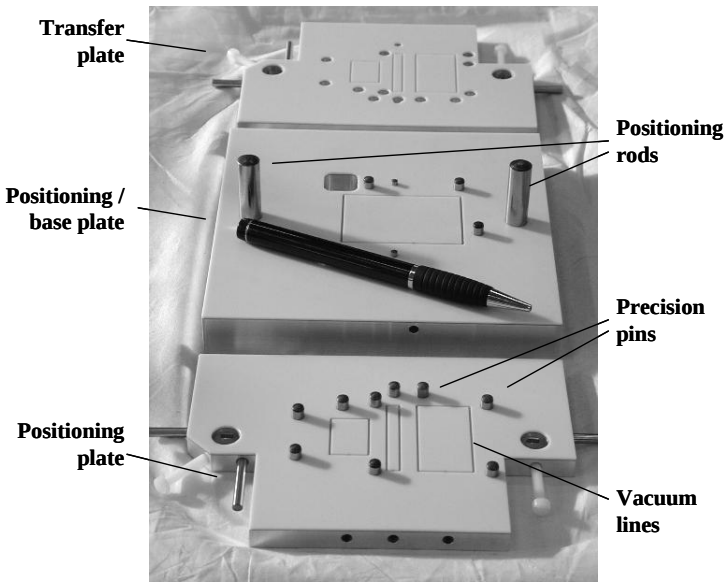

Figure 2.14 Assembly tooling for the prototype module with a small sensor, which consists of one base plate, one positioning plate and one transfer plate. The tooling has a repeatibility better than 3 μm.

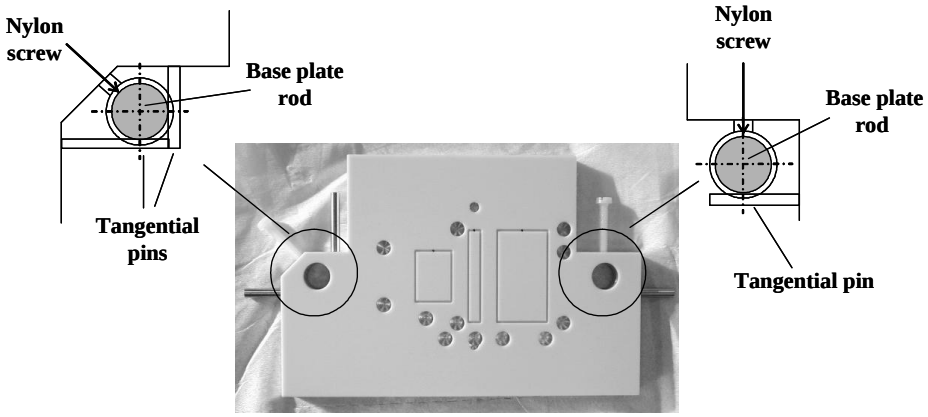

Figure 2.15 Mechanism to position the transfer plate with respect to the base plate, based on precision pins which are tangential to the base plate rods.

The mechanical prototype module is glued in two steps: in a first step the readout electronics and the sensor are glued to the support plate; in a second step, the spacer and pitch adapter are glued to the support plate. The Araldite® 2011 epoxy, which was used to glue the prototypes, needs about 10 hours to cure at an ambient temperature of 23 °C. Therefore, a full module could be assembled within two days. At that moment bonding and soldering of the high voltage coaxial lines can be done. When gluing real components the number of steps is increased to three, since the hybrid cannot be glued until the sensor has been assembled.

The first gluing step of the mechanical prototype module is shown in Figure 2.16. First of all, the silicon detector and alumina hybrid components are positioned against the alignment pins on the positioning plate (1), which is actually sitting on top of the base plate. Once positioned and kept in place by vacuum, the two components are picked with the transfer plate (2), which is fixed with the

nylon screws (3). Then vacuum is made on this plate (4) and the glue is applied. Afterwards, the silicon support plate is placed on the base plate (5). Finally, the detector and hybrid are glued to the support plate (6).

In a second gluing step the CFC spacer and the pitch adapter are glued. The pitch adapter is positioned and transferred following steps (1) to (4). At this point, the glue is applied on one side of the CFC spacer, and positioned on top of the support plate using the precision pins at the alignment hole and slot. Afterwards, the glue is applied on the pitch adapter and then the transfer plate is placed on top of the spacer.

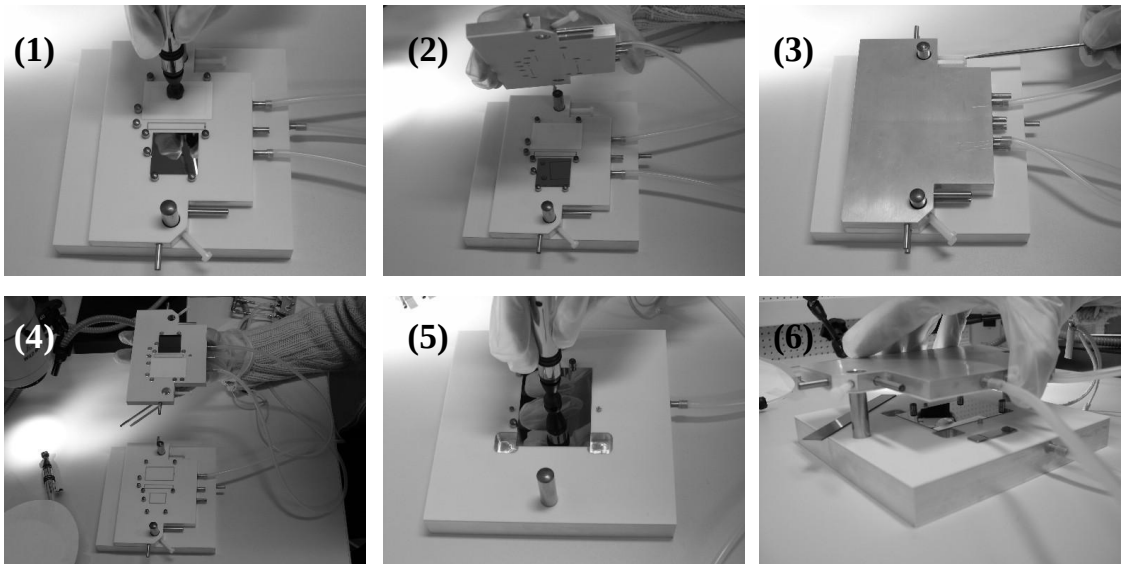

Figure 2.16 The assembly of a prototype module is done using positioning and transfer plates.

A second set of tooling was designed and produced in order to assemble the silicon microstrip detector module with a large sensor (Figure 2.1). The design of the transfer plates (Figure 2.17) is more sophisticated since real components are used now. The gluing must be done in three steps since the silicon sensor needs to be glued before the readout electronics. Therefore, one more transfer plate is needed.

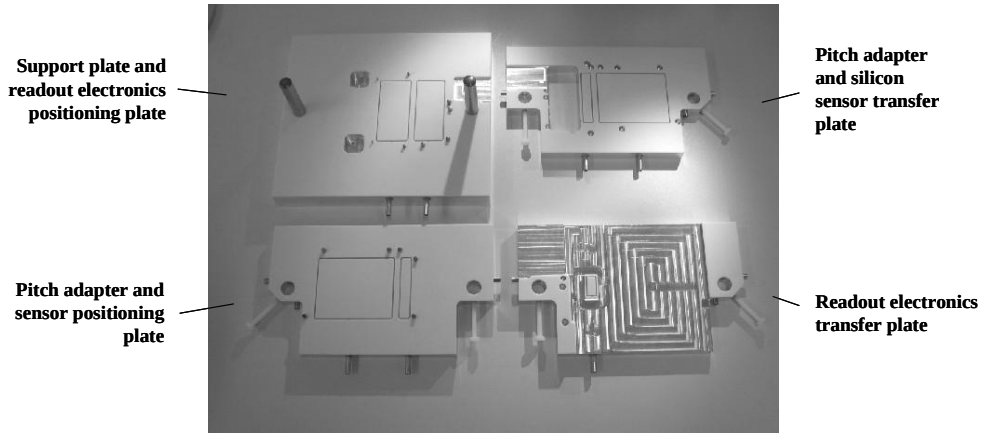

Figure 2.17 The assembly tooling for the module with a large sensor, which consists of two transfer and two positioning plates.

Spacer assembly tooling

Before the module assembly, the cooling pipes are embedded into a carbon fibre composite (CFC) structure of the spacer, which is placed under the pitch adapter, as shown by Figure 2.2. A special tooling was designed and produced for this purpose.

The CFC spacer is made out of three pieces which are joined together by two capillary pipes, as was shown in Figure 2.2. The glue is first distributed under the microscope along the grooves which are machined on the CFC pieces to hold the pipes. The pieces themselves do not need to be assembled with high precision, since the position of the cooling pipe is not crucial and the precision hole and slot on the CFC are aligned with respect to the detector while gluing the spacer to the support plate with the assembly tooling.

However, the spacer assembly tooling should favour that all the surface of the cooling pipe is in contact with the CFC through a continuous film of glue. This is achieved by gluing the components while pressing from the sides (see Figure 2.18). The pitch adapter lies on top of the spacer and therefore should be horizontal. That is the reason why, despite the fact that one cooling pipe is sufficient from a thermal point of view, a second cooling pipe is also integrated in the structure, being effectively a shim for the spacer.

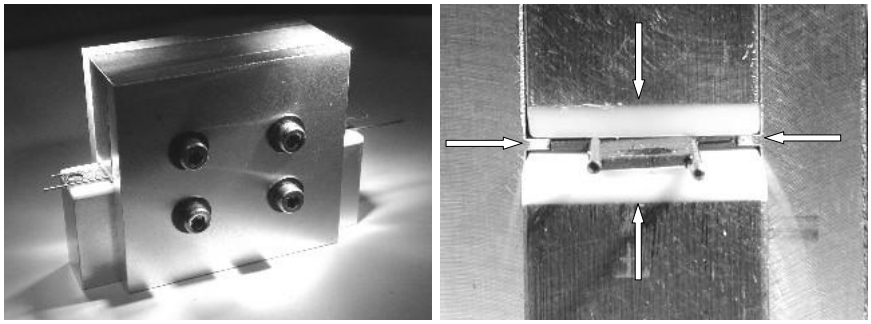

Figure 2.18 Assembly tools for carbon fiber composite spacer (left) and detail of the 0.6 mm outer diameter capillary pipes embedded in the structure (right).

Alignment of the silicon detector module with respect to the beam

The alignment of the cold microstrip silicon detector module with respect to the beam and to the other detectors is achieved by using a warm support plate which is positioned with precision pins on a stable mechanical structure (i.e. a vacuum chamber such as a Roman Pot). The cold module itself is attached to this support plate using three thermally isolating precision support posts (Figure 2.19).

The 2 mm diameter cold dowels align the module via its precision holes. The dowels sit on top of a thin-wall cylinder, the other end of which is welded to a second concentric one, as shown by the drawing of Figure 2.19. The dowels end with a threaded part on which a nut is tightened for clamping the module. This re-entrant structure is welded to a flange that has two precision holes and two threaded ones, used for precision positioning and fixation to the support plate, respectively.

To avoid a large heat leak from the support plate at room temperature to the silicon module at 130 K, the support posts are made of low-conductivity stainless steel. Besides, the length of the thermal path between the flange and the cold dowels is maximized by using cylinders with thin walls in the re-entrant structure. Moreover, the support post must not only ensure precision on the position and

therefore it has to be rigid enough to carry the weight of the module without large deformation but also needs to be elastic enough to prevent the development of thermal stress during cool down, thus avoiding the silicon module breaking.

Several pin geometries (length of concentric cylinders and their wall thickness) were simulated. The external cylinder has 5 mm outer diameter and the inner one 4 mm outer diameter. Both cylinders have a wall thickness of 0.1 mm and their respective lengths are 15 and 20 mm. The total length of the support post is 23 mm. The thermal and mechanical properties of stainless steel were extracted from the Brookhaven National Laboratory Selected cryogenic data notebook [17] and therefore thermal conductivity and thermal dilatation were considered as a function of temperature in the simulation.

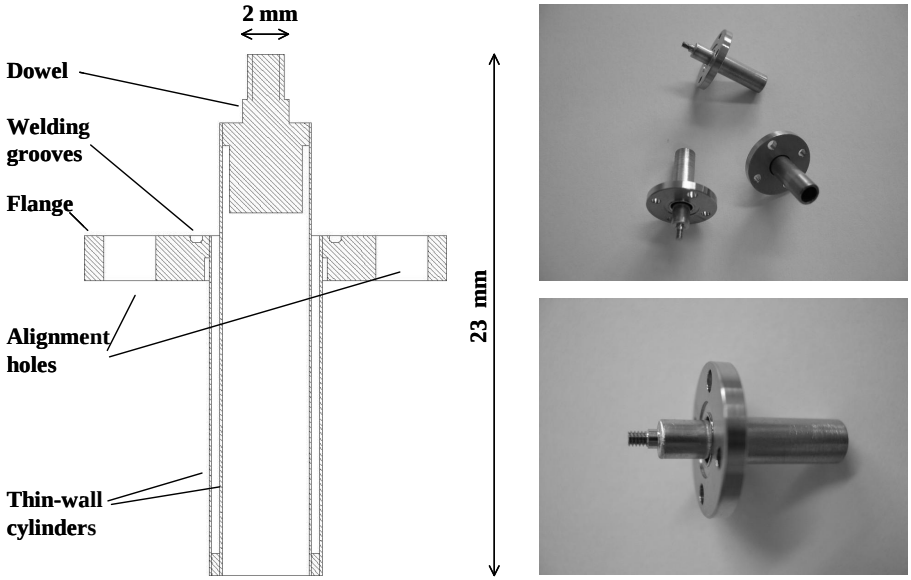

Figure 2.19 Thermally isolating precision support posts used to align the cold module with respect to a warm support plate.

Considering a constant temperature of 300 K on the flange which is in contact with the support structure, and 130 K on the dowel which is in direct contact with the module, the heat leak from the warm part to the module is about 30 mW. The thermal contractions on the inner stainless steel cylinder are of a few micrometers. The Von Mises stress distribution shows how the maximum stresses are located on the precision holes of the flange, as could be expected, since it is at this point where the constraints are applied. The Young modulus of stainless steel is considered to be of 200 GPa (constant with temperature) and the yield strength is around 290 MPa. The maximum thermal stress shown by the simulation is smaller than 40 MPa, and therefore negligible.

The vacuum chamber

Following the thermal and alignment principles described above, a vacuum chamber to host a cryogenic module was designed and produced in collaboration with the Central Cryogenic Laboratory at CERN. As can be seen in Figure 2.20, the cryogenic module is fixed through three isolating precision support posts to a warm plate, which is attached to the vacuum vessel with three support rods. The cryostat covers are equipped with windows, making this setup suitable for test beam experiments. The cooling

can be done either with liquid nitrogen or any fluid pumped in a closed cycle system such as the one described in Section 2.3.

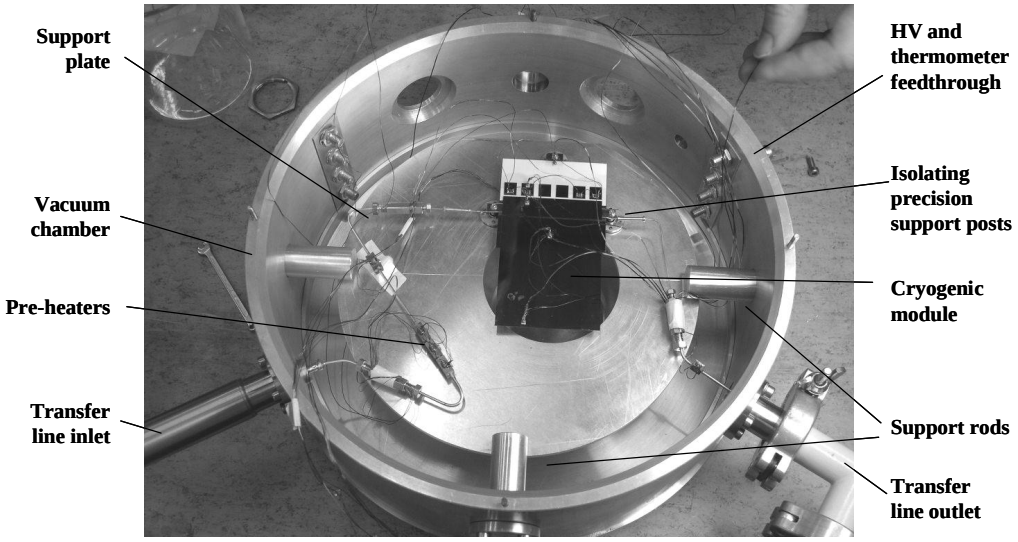

Figure 2.20 Vacuum chamber hosting a module with a large sensor.

Assembly of a first mechanical prototype

Several mechanical prototypes of Roman Pot modules, made out of the same materials as the real components and based on the principles described above in this chapter, were assembled using the precision tooling (Figure 2.21). All these mechanical modules were thermally cycled ten times from 300 K to 77 K without breaking the silicon, corroborating that the glue layer thickness is suitable to avoid fatal stress in the silicon. This finding was confirmed by quantitative studies described in the next chapter.

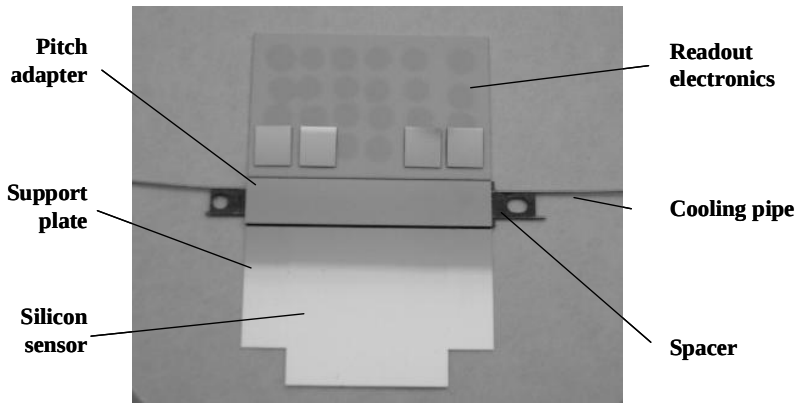

Figure 2.21 Mechanical module prototype built using the assembly tooling.